SANDIA REPORT
SAND2003-8412
Unlimited Release
Printed September 2003

A Numerical Scheme for Modelling Reacting Flow with Detailed Chemistry and Transport

H.N. Najm, O.M. Knio, and P.H.Paul

Prepared by
Sandia National Laboratories
Albuquerque, New Mexico 87185 and Livermore, California 94550

Sandia is a multiprogram laboratory operated by Sandia Corporation, a Lockheed Martin Company, for the United States Department of Energy's National Nuclear Security Administration under Contract DE-AC04-94AL85000.

Issued by Sandia National Laboratories, operated for the United States Department of Energy by Sandia Corporation.

Available to DOE and DOE contractors from
U.S. Department of Energy
Office of Scientific and Technical Information
P.O. Box 62
Oak Ridge, TN 37831

Telephone: (865)576-8401
Facsimile: (865)576-5728
E-Mail: reports@adonis.osti.gov
Online ordering: http://www.doe.gov/bridge
Available to the public from
U.S. Department of Commerce
National Technical Information Service
5285 Port Royal Rd
Springfield, VA 22161

Telephone: (800)553-6847
Facsimile: (703)605-6900
E-Mail: orders@ntis.fedworld.gov
Online order: http://www.ntis.gov/help/ordermethods.asp?loc=7-4-0#online

SAND2003-8412

SAND2003-8412
Unlimited Release
Printed September 2003

A Numerical Scheme for Modelling Reacting Flow with Detailed Chemistry and Transport

H.N. Najm
Combustion Research Facility
Sandia National Laboratories
Livermore, CA

O.M. Knio
The Johns Hopkins University
Baltimore, MD

and

P.H. Paul
Eksigent Technologies LLC
Livermore, CA

Abstract

An efficient projection scheme is developed for the simulation of reacting flow with detailed kinetics and transport. The scheme is based on a zero-Mach-number formulation of the compressible conservation equations for an ideal gas mixture. It is a modified version of the stiff operator-split scheme developed by Knio, Najm & Wyckoff (1999, J. Comput. Phys. 154, 428). Similar to its predecessor, the new scheme relies on Strang splitting of the discrete evolution equations, where diffusion is integrated in two half steps that are symmetrically distributed around a single stiff step for the reaction source terms. The diffusive half-step is integrated using an explicit single-step, multistage, Runge-Kutta-Chebyshev (RKC) method, which replaces the explicit, multi-step, fractional sub-step approach used in the previous formulation. This modification maintains the overall second-order convergence properties of the scheme and enhances the efficiency of the computations by taking advantage of the extended real-stability region of the RKC scheme. Two additional efficiency-enhancements are also explored, based on an extrapolation procedure for the transport coefficients and on the use of approximate Jacobian data evaluated on a coarse mesh. By including these enhancement schemes, performance tests using 2D computations with a detailed C_1C_2 methane-air mechanism and a detailed mixture-averaged transport model indicate that speedup factors of about 15 are achieved over the previous split-stiff scheme.

Introduction

The modelling of chemically reacting flow presents difficulties associated with the large range of spatial and temporal scales involved. The large range of length scales leads to fine spatial resolution requirements and a large number of mesh points. The large range of time scales, and the corresponding stiffness of the governing equations, results in significant challenges to time integration schemes, and typically leads to very small time step limitations in explicit schemes.

Stiffness limitations are typically overcome by adopting a stiff integration scheme or a specially-tailored integration method. A variety of approaches have been used to construct different classes of stiff solvers. These were reviewed in detail in our earlier works [1,2]. It should be emphasized, however, that incorporation of a stiff solver into a reacting flow code is not straightforward, in large part because of the coupling between the reaction term and the diffusion and convective transport terms. The presence of convective terms is least problematic, since explicit treatments with CFL numbers [3, 4] below unity are in most cases suitable. The treatment of the diffusion term, on the other hand, is a more delicate issue. In many situations, an implicit treatment of diffusion provides a suitable means for avoiding the restrictive stability limitations of explicit solvers. For detailed reacting flow models, however, diffusion coefficients exhibit a non-linear dependence on temperature and on species concentrations, and this dependence couples the diffusion terms in all the scalar evolution equations. In two and three dimensions, this leads to a very large system of coupled non-linear equations, whose solution poses significant challenges.

The above considerations suggest that hybrid implicit-explicit (IMEX) approaches, in which individual terms in the governing equations are integrated using specialized schemes, may be particularly advantageous (see discussion in [1, 2]). Our previous work [1] used a semi-implicit, additive, stiff scheme for the simulation of 2D reacting flow with detailed kinetics. The numerical formulation in [1] uses a predictor-corrector methodology; the predictor uses an explicit linear multi-step method while the corrector incorporates a stiff method for the treatment of chemical source terms. The scheme was applied to the simulation of premixed methane-air flames [5]. The computations have shown that the scheme efficiently overcomes the chemical stiffness of the equations of motion and results in significant speed-up over its explicit predecessor. However, since the diffusion terms are handled explicitly, the time step could not be increased beyond the diffusion stability limit.

This limitation was overcome in [2] using a second-order operator-split time integration procedure, with fractional stepping in the diffusional half-steps. One of the advantages of operator-splitting techniques stems from the sequential application of individual operators, which enables independent optimization of the integration procedure over each split step and, consequently, enhancement of the efficiency of the computations. Operator-splitting techniques have been widely utilized in atmospheric modelling studies [6–13] to decouple reaction from diffusion and convection terms, diffusion+reaction from convection, and to decouple operators in different spatial dimensions. To date, the symmetric Strang [14] splitting approach for achieving second-order accuracy has been most commonly and successfully used. Higher-order splitting approaches have been reported [6, 15–17], but have generally been found to exhibit considerable stability-related problems due to negative time stepping. For additional discussion of the stability of operator-split schemes see [6, 17, 18].

The success of the operator-splitting approach in [2] hinged on the expectation that evaluation of the diffusion source terms is much cheaper than that of the chemical source terms. This allowed the use of multiple fractional time steps within each diffusional half-step, requiring repeated evaluations of the diffusional source terms in each global time step. While increasing the number of fractional diffusional steps leads to larger global time steps, and in most cases more efficient computations, inherent limitations to this approach exist. By increasing the number of fractional diffusion steps, the global time step increases and splitting errors increase as well. Thus, accuracy requirements force an upper limit on the global time step and consequently on the number of fractional steps. Moreover, as the number of diffusional fractional steps is increased, diminishing returns to code speedup are observed as the cost of repeated fractional-step integration of diffusion becomes comparable to, or larger than the chemistry integration cost. When this balance is approached, the use of additional fractional steps to increase the overall time step becomes counter-productive.

Furthermore, when the costs of evaluating transport properties are significant, the splitting procedure introduced in [2] may lose most of its advantages and cease to be attractive. For example, we have found that when the simplified transport model used in [1, 2] was generalized in order to account for the dependence of the transport coefficients on the mixture composition, a 50% increase in computational costs are observed in

the context of a semi-implicit IMEX construction [1], while a factor of 6 increase in computational cost is observed with an operator-split [2] implementation using 16 fractional diffusion steps. Due to their exorbitant cost, we find that the use of detailed transport models –that locally evaluate transport coefficient based on local mixture concentrations– is not practical with either of our previous constructions.

One should note, however, that the use of detailed transport and chemical models in transient multi-dimensional simulation have previously been attempted. For example, Day and Bell [19] incorporate the split construction in [2] into reacting flow computations using detailed chemical and transport model adapted from Chemkin [20]. However, their implementation focused on the development of an adaptive-grid methodology and did not specifically address the cost of transport properties. In the present work, we tackle this difficulty by using (1) a more efficient extended-stability Runge-Kutta-Chebyshev (RKC) time stepping procedure [21] in each diffusional half-step, and (2) an efficient extrapolation procedure for transport properties which retains the convergence properties of the original scheme but requires only one direct evaluation of transport properties in each global time step. With this combination, we demonstrate 2D methane-air flame-vortex-pair computations with GRImech1.2 kinetics [22] and a full mixture-averaged transport property model [23, 24].

The construction and properties of RKC schemes have been extensively discussed in the literature. These schemes have been designed for the explicit time integration of stiff ODE systems originating from spatial discretization of parabolic PDEs [25–28]. They are a typical example of explicit, stabilized RK schemes [29–37], in which additional internal stages are utilized to increase the stability boundary of the scheme. The schemes exhibit an extended real stability interval which grows quadratically with the number of stages. This feature enables careful and efficient adjustment of the number of stages so as to achieve a target stability region, so that the global time step can be selected based essentially on accuracy considerations. Typically, a stabilized RK scheme involves a small number of function evaluations which ensure an order of accuracy, while the rest are relevant to the stability properties. Economized schemes have been developed which use cheaper approximate function evaluations in the latter stages, without degrading the overall accuracy of the integration scheme [38]. The present RKC-scheme formulation is based on the construction presented in [21], which uses the three-term Chebyshev recursion of van der Houwen and Sommeijer [25]. It utilizes a single-step, multi-stage, second-order construction using the Bakker-Chebyshev polynomial [30, 39, 40] and, as outlined below, implements damping to provide a narrow stable strip region along the negative real axis [25, 41].

The paper is organized as follows. In section 2, we provide a brief overview of the governing equations for zero-Mach-number combustion, and of the chemical and transport models. In section 3, we describe the RKC operator-split implementation and the numerical procedure for extrapolation of transport properties. Results are presented in section 4. The performance of the present scheme is first examined based on computational tests of a one-dimensional, nonlinear reaction-diffusion equation. The tests are used to establish the convergence properties of the scheme and briefly analyze the effect of numerical parameters. The full scheme is then applied to the simulation of premixed methane-air flames in one and two space dimensions. These tests are used to amplify the results of the idealized analysis and to investigate the speedup gained in the computations. Major conclusions are given in section 5.

1 Formulation

The physical model used in the present study is based on extending the formulation developed in [1, 2]. The model relies on the zero-Mach-number limit of the compressible conservation equations [42]. In this limit, acoustic waves are ignored and the pressure field is decomposed into a spatially-uniform component $P_0(t)$ and a hydrodynamic component $p(x,t)$ which varies in space and time. The model assumes a gas mixture with zero bulk viscosity [43], and ignores Soret and Dufour effects [44], as well as body forces and radiant heat transfer.

1.1 Governing equations

Under the above assumptions, the non-dimensional governing equations are expressed as:

$$\frac{\partial \rho}{\partial t} + \nabla \cdot (\rho v) = 0 \tag{1}$$

$$\frac{\partial(\rho u)}{\partial t} + \frac{\partial(\rho u^2)}{\partial x} + \frac{\partial(\rho uv)}{\partial y} = -\frac{\partial p}{\partial x} + \frac{1}{\mathrm{Re}}\Phi_x \tag{2}$$

$$\frac{\partial(\rho v)}{\partial t} + \frac{\partial(\rho vu)}{\partial x} + \frac{\partial(\rho v^2)}{\partial y} = -\frac{\partial p}{\partial y} + \frac{1}{\mathrm{Re}}\Phi_y \tag{3}$$

$$\frac{\partial T}{\partial t} + v \cdot \nabla T = \frac{1}{\mathrm{Re\,Pr}} \frac{\nabla \cdot (\lambda \nabla T)}{\rho c_p} + \frac{1}{\mathrm{ReSc}} \frac{Z \cdot \nabla T}{c_p} + \mathrm{Da} \frac{w_T}{\rho c_p} \tag{4}$$

$$\frac{\partial(\rho Y_i)}{\partial T} = -\nabla \cdot (\rho v Y_i) - \frac{1}{\mathrm{ReSc}} \nabla \cdot (\rho Y_i V_i) + \mathrm{Da}\, w_i \tag{5}$$

respectively. Here, ρ is the density, T is the temperature, $v = (u, v)$ is the velocity vector, Y_i is the mass fraction of species i, μ is the dynamic viscosity, λ is the thermal conductivity, c_p is the mixture specific heat, w_i is the chemical production rate of species i, w_T is rate of chemical heat release, $Z \equiv -\sum_{i=1}^{N} c_{p,i} V_i$, V_i is the diffusion velocity of species i, $c_{p,i}$ is the heat capacity of species i, Re, Pr, Sc, and Da are the Reynolds, Prandtl, Schmidt, and Damköhler numbers respectively, while Φ_x,Φ_y are the viscous stress terms.

The mixture is assumed to obey the perfect gas law, with individual species molecular weights, specific heats, and enthalpies of formation. The equation of state is expressed as:

$$P_0 = \rho T / \overline{W} \tag{6}$$

where $\overline{W} \equiv 1/\left(\sum_{i=1}^{N} Y_i / W_i\right)$ is the local molar mass of the mixture, N is the total number of species, and W_i is the molecular weight of species i. Note that for an open domain P_0 is constant. The specific heat of the mixture is given by:

$$c_p = \sum_{i=1}^{N} Y_i c_{p,i} \tag{7}$$

where $c_{p,i}$ is the specific heat of the i-th species at constant pressure.

For the purpose of the numerical implementation described below, the time rate of change of density is found by differentiating the equation of state,

$$\frac{\partial \rho}{\partial t} = \rho \left(-\frac{1}{T}\frac{\partial T}{\partial t} - \overline{W} \sum_{i=1}^{N} \frac{1}{W_i} \frac{\partial Y_i}{\partial t} \right) \tag{8}$$

and substituting for $\partial T/\partial t$ and $\partial Y_i/\partial t$ from equations (4) and (5), respectively.

1.2 Kinetic Model

A detailed kinetic model with K elementary reactions is assumed. The production rate for each species (w_i) is given by the sum of contributions of elementary reactions [44], with Arrhenius rates $r_k = A_k T^{b_k} e^{-E_k/RT}$, $k = 1, \ldots, K$. The overall progress of an elementary reaction accounts for both forward and backward rates, corrections for third body efficiencies, and pressure dependence [20]. The heat release rate term is given by:

$$w_T = -\sum_{i=1}^{N} h_i w_i \tag{9}$$

where $h_i = h_i^o + \int_{T^o}^{T} c_{p,i} dT$ is the enthalpy of species i, and the superscript o is used to denote known reference conditions. In the computations below, we focus on the GRImech1.2 C_1C_2 mechanism [22], which involves 32 species and 177 elementary reactions, i.e. $N = 32$ and $K = 177$.

1.3 Transport Models

In our previous implementations, we had relied on a simplified transport model which takes advantage of the fact that the N-th species (in our case N_2) is dominant, and consequently approximates the diffusion velocity of any other species $i \neq N$ in the mixture by $V_i = -D_{iN}\nabla Y_i/Y_i$, where D_{iN} is the binary mass diffusion coefficient of species i into the N-th species at the mixture local temperature and stagnation pressure. V_N is found from the identity $\sum_{i=1}^{N} Y_i V_i \equiv 0$ [44]. Similarly, the mass fraction Y_N is obtained from the identity $\sum_{i=1}^{N} Y_i \equiv 1$. Note that the above approximation of V_i assumes that $Y_i \ll Y_N$, $i = 1,\ldots,N-1$, i.e. that species $i = 1,\ldots,N-1$ are traces in species N. In addition, for the purpose of computational efficiency, the simplified transport model also sets the mixture transport properties (μ,λ) equal to those of the dominant species at the local temperature.

As mentioned in the introduction, one of the objectives of the present work is to explore an efficient implementation of a more elaborate transport model. In this work, we use a mixture-averaged transport model implemented using the Dipole Reduced Formalism (DRFM) [23, 24]; the formulation is outlined below.

The mixture viscosity is given by the Wilke'50 formula [23]:

$$\eta_{\text{mix}} = \sum_{i=1}^{N} \frac{X_i \eta_i}{X_i + \sum_{j\neq i} X_j \Phi_{ij}} \tag{10}$$

where X_i is the mole fraction of species i,

$$\Phi_{ij} = \frac{\left[1 + \left(\frac{W_j}{W_i}\right)^{\frac{1}{4}} \left(\frac{\eta_i}{\eta_j}\right)^{\frac{1}{2}}\right]^2}{8\left(1 + \frac{W_i}{W_j}\right)^{\frac{1}{2}}}, \tag{11}$$

W_i is the molar mass of species i,

$$\eta_i = \frac{5}{16}\left(\frac{W_i k_B T}{\pi}\right)^{\frac{1}{2}} \frac{1+h_i}{\sigma_{ii}^2 \Omega_{ii}^{(2,2)^*}} \tag{12}$$

is the pure component shear viscosity of species i, where the second-order correction h_i (neglected in our first-order formulation) is a function of temperature and pure species identity, k_B is Boltzmann's constant, T is temperature, and σ_{ij} is the Lennard-Jones radius for i–j collisions $\sigma_{ij} = (\sigma_i + \sigma_j)/2$. Further, $\Omega_{ij}^{(2,2)^*}$ and $\Omega_{ij}^{(1,1)^*}$ (below) are collision integrals that are functions of temperature and pure species identity. Thus, $\eta_i = \eta_i(T)$, and $\Phi_{ij} = \Phi_{ij}(T)$.

The mixture thermal conductivity is given by [45]:

$$\lambda_{\text{mix}} = \sum_{i=1}^{N} \frac{X_i \lambda_i}{X_i + 1.065 \sum_{j\neq i} X_j \Phi_{ij}} \tag{13}$$

where Φ_{ij} is that given above, and $\lambda_i = P_i \lambda_i^{(m)}$. $\lambda_i^{(m)}$ is a hypothetical thermal conductivity of species i, based on the molecular gas behaving like a monatomic/translational gas, such that

$$\lambda_i^{(m)} \equiv \frac{15 k_B \eta_i}{4 W_i}, \tag{14}$$

and $P_i = P_i(T)$ is a known polynomial fit (see the related discussion in the Appendix).

Finally, the mixture-averaged mass diffusion coefficient of species i into the mixture is given by

$$D_{i,\text{mix}} = \frac{\sum_{j\neq i} X_j W_j}{\overline{W} \sum_{j\neq i} X_j / D_{ij}} \tag{15}$$

where $\overline{W} = \sum_{j=1}^{N} X_j W_j$ is the molar mass of the mixture, expressed here in terms mole fractions,

$$D_{ij} = D_{ji} = \frac{3}{8n}\left(\frac{k_B T}{2\pi W_{ij}}\right)^{\frac{1}{2}} \frac{1+d_{ij}}{\sigma_{ij}^2 \Omega_{ij}^{(1,1)^*}}, \tag{16}$$

is the binary diffusion coefficient of species i into species j, $W_{ij} = W_i W_j/(W_i + W_j)$,

$$n = \frac{P_0}{k_B T} \tag{17}$$

is the total number density and P_0 is the pressure. The second-order correction d_{ij} (neglected in our first-order formulation) introduces a mole-fraction dependence into D_{ij}.

Thus, for constant pressure, and when d_{ij} is neglected, $D_{ij} = D_{ij}(T)$. The Soret (i.e. thermal diffusion) and Dufort effects are inherently second-order transport properties that are properly neglected in our first-order transport model. In our formulation, the mixture viscosity, thermal conductivity, and the species diffusivities into the mixture are functions of the set of mole fractions and the corresponding pure (or binary) species properties $\eta_i(T)$, $\lambda_i(T)$ and $D_{ij}(T)$.

Finally, neglecting "pressure" and thermal diffusion [46, 47], the diffusion velocity V_i (Eq. 5) is defined in terms of the $D_{i,\mathrm{mix}}$ coefficients as follows. For $i = 1 \ldots N-1$,

$$\begin{aligned} Y_i V_i &= -\frac{Y_i}{X_i} D_{i,\mathrm{mix}} \nabla X_i & (18)\\ &= -D_{i,\mathrm{mix}} \nabla Y_i - D_{i,\mathrm{mix}} \frac{Y_i}{\overline{W}} \nabla \overline{W} & (19) \end{aligned}$$

where we have used the identity $Y_i/X_i = W_i/\overline{W}$; and, $Y_N V_N$ is given by:

$$Y_N V_N = 1 - \sum_{i=1}^{N-1} Y_i V_i. \tag{20}$$

Note that the limit of a dilute mixture with a single dominant N-th species is retrieved as $\nabla \overline{W} \to 0$ and $D_{i,\mathrm{mix}} \to D_{i,N}$.

The implementation of the above transport properties in the operator-split fractional step construction in [2] leads to a substantial increase in computational effort which, as noted in the introduction, renders the computations impractical. To illustrate the scaling of computational complexity, consider the operator-split construction using M fractional steps in the original scheme (or stages in the present implementation) for scalars. For N-species, the evaluation of λ at a point in space requires $O(N^2)$ work. Similarly, each mixture-averaged diffusion coefficient D_{ij} requires $O(N)$ work, and with N such evaluations, we have $O(N^2)$ work requirement for $\mathbf{D} = \{D_{i,\mathrm{mix}}\}$. As a result, the operation count per time step per mesh cell, relevant to transport property evaluation, is $O(2MN^2)$, hence the significant rise in transport costs with increasing number of steps/stages.

While the RKC construction described below is more efficient than the fractional stepping procedure in [2], the problem remains that a multistage implementation involves significant cost penalties associated with detailed transport. In the present work, we explore an extrapolation procedure for the transport properties in order to reduce these costs. The extrapolation procedure can be implemented with either the RKC or fractional stepping context, but the RKC-extrapolation combination clearly provides better efficiency. The formulation of the extrapolation scheme is outlined towards the end of the following section.

2 Numerical Scheme

As mentioned in the introduction, the primary objective of the present effort is to enhance the performance of our previous operator-split, stiff scheme [2], particularly regarding the fractional integration of diffusion source terms. To this end, we start with a brief outline of the previous construction and then provide a description of the enhanced solver.

The stiff-split scheme developed in [2] is based on a projection method [48–55] for reacting flow. The formulation, which follows the construction outlined in [1], assumes an open 2D domain and relies on a second-order centered finite-difference discretization of the equations of motion. Field variables are discretized using a staggered grid with uniform cell size along each coordinate direction. Velocity components are specified at cell edges, while scalar variables are specified at cell centers. Numerical integration of the discretized equations of motion is based on a predictor-corrector integration approach. The predictor stage relies on a symmetrically-split, stiff formulation in which advection and diffusion terms are treated explicitly in fractional steps that are symmetrically distributed around stiff integration of chemical source terms. The stiff integration is adapted from the DVODE integration package [56], and uses an analytical Jacobian formulation. Numerical integration of the momentum equations involves a pressure correction step which requires the inversion of a pressure Poisson equation; where we use a fast FFT Poisson solver. The predictor step is followed by an explicit corrector step that enhances the coupling between the velocity, density and hydrodynamic pressure fields and, consequently, the stability of the computations [57, 58].

In [2], the fractional step integration of the diffusion and transport terms is based on an explicit second-order Runge-Kutta and Adams-Bashforth schemes. The stability of the fractional step integration is restricted by the diffusion stability limit. For well-resolved flame fronts, mesh sizes on the order of 15 μm are necessary. Consequently, the critical diffusion time step is substantially smaller than the time steps allowed by the stiff integration. As a result, it proves advantageous to distribute diffusion sub-steps around a single stiff integration update of the reaction source terms. While this approach results in substantial enhancement in the performance of the code, the computational tests detailed in [2] reveal that the cost associated with the repeated fractional step integration of diffusion eventually becomes the factor limiting the efficiency of the calculations, even with very simple transport property models.

With the present shift towards more detailed transport models, it becomes essential to explore means to overcome the above limitation. Our approach is based on replacing the RK2/AB2 treatment of diffusion with the Runge-Kutta-Chebyshev (RKC) scheme that is adapted from [21, 25, 27, 28]. As discussed earlier, RKC is an explicit, predictor-corrector method that exhibits an extended-stability region along the negative real axis, and thus appears ideally suited for the present objective.

In order to outline the incorporation of the RKC scheme into the split-stiff formulation, we first recast the governing equations into the following form:

$$\frac{\partial(\rho Y_i)}{\partial t} = L_i \equiv C_i + R_i + D_i \tag{21}$$

$$\frac{\partial \rho}{\partial t} = C_\rho + R_\rho + D_\rho - C_{W,C} - C_{W,R} - C_{W,D} \tag{22}$$

$$\frac{\partial(\rho v)}{\partial t} = N(\rho, v) + F(\mu, v) - \nabla p \tag{23}$$

where $N(\rho, v)$ is the momentum convection term, $F(\mu, v)$ is the viscous force term, while

$$\begin{aligned}
C_i &\equiv -\nabla \cdot (\rho v Y_i) \\
R_i &\equiv \mathrm{Da}\, w_i \\
D_i &\equiv -\frac{1}{\mathrm{Re}\,\mathrm{Sc}} \nabla \cdot (\rho Y_i V_i), \\
C_\rho &\equiv \frac{\rho}{T} v \cdot \nabla T \\
R_\rho &\equiv -\frac{1}{c_p T} \mathrm{Da}\, w_T \\
D_\rho &\equiv -\frac{1}{\mathrm{Re}\,\mathrm{Pr}\, c_p T} \nabla \cdot (\lambda \nabla T) + \frac{\rho}{T} \frac{1}{c_p \mathrm{Re}\,\mathrm{Sc}} Z \cdot \nabla T
\end{aligned}$$

and

$$
\begin{aligned}
C_{W,C} &\equiv \overline{W}\sum_{i=1}^{N} -\frac{\rho v\cdot\nabla Y_i}{W_i} \\
C_{W,R} &\equiv \overline{W}\sum_{i=1}^{N} \frac{\mathrm{Da}\, w_i}{W_i} \\
C_{W,D} &\equiv -\overline{W}\sum_{i=1}^{N} \frac{1}{W_i}\frac{1}{\mathrm{Re}\,\mathrm{Sc}}\nabla\cdot(\rho Y_i V_i)
\end{aligned}
$$

Using these definitions, the implementation of the extended RKC solver can be summarized as follows.

Stiff Predictor

The present construction maintains the operator-split construction in [2], but the treatment of diffusion terms is performed using RKC time integration instead of repeated application of AB2. Convection terms are still treated explicitly using AB2, and the resulting source terms are spread evenly among the split time steps. Diffusion terms are integrated with RKC over two half-time-steps separated by a chemistry term integration over a full time-step. The procedure is as follows.

S1. Explicit convection source terms for the species (C_i^e) and density (S_ρ^e) evolution equations are evaluated. We rely on the explicit AB2 scheme and set:

$$C_i^e = \frac{3}{2}C_i^n - \frac{1}{2}C_i^{n-1} \tag{24}$$

$$S_\rho^e = \frac{3}{2}\left(C_\rho^n - C_{W,C}^n\right) - \frac{1}{2}\left(C_\rho^{n-1} - C_{W,C}^{n-1}\right) \tag{25}$$

S2. The diffusion term is integrated over a step size of $\Delta t/2$ using a slightly-damped, single-step, S-stage ($S \geq 2$), second-order RKC scheme. The starting values (superscript 0) are the scalar fields at the beginning of the time step:

$$\rho^0 = \rho^n \tag{26}$$

$$(\rho Y_i)^0 = (\rho Y_i)^n \tag{27}$$

$$T^0 = T^n \tag{28}$$

The RKC integration stages are then given by [21]:

$$\rho^1 = \rho^0 + \tilde{\eta}_1\frac{\Delta t}{2}\left(D_\rho^0 - C_{W,D}^0 + \frac{1}{2}S_\rho^e\right) \tag{29}$$

$$(\rho Y_i)^1 = (\rho Y_i)^0 + \tilde{\eta}_1\frac{\Delta t}{2}\left(D_i^0 + \frac{1}{2}C_i^e\right) \tag{30}$$

$$T^1 = \frac{P_0\overline{W}^1}{\rho^1} \tag{31}$$

and

$$
\begin{aligned}
\rho^s &= (1-\eta_s-\nu_s)\rho^0 + \eta_s\rho^{s-1} + \nu_s\rho^{s-2} \\
&+ \tilde{\eta}_s\frac{\Delta t}{2}\left(D_\rho^{s-1} - C_{W,D}^{s-1} + \frac{1}{2}S_\rho^e\right) + \tilde{\gamma}_s\frac{\Delta t}{2}\left(D_\rho^0 - C_{W,D}^0 + \frac{1}{2}S_\rho^e\right) \qquad (32) \\
(\rho Y_i)^s &= (1-\eta_s-\nu_s)(\rho Y_i)^0 + \eta_s(\rho Y_i)^{s-1} + \nu_s(\rho Y_i)^{s-2} \\
&+ \tilde{\eta}_s\frac{\Delta t}{2}\left(D_i^{s-1} + \frac{1}{2}C_i^e\right) + \tilde{\gamma}_s\frac{\Delta t}{2}\left(D_i^0 + \frac{1}{2}C_i^e\right) \qquad (33) \\
T^s &= \frac{P_0\overline{W}^s}{\rho^s} \qquad (34)
\end{aligned}
$$

for $s = 2, \ldots, S$. The constants appearing in the RKC integration stages are given by [21]:

$$w_0 = 1 + \frac{\varepsilon}{S^2}, \quad w_1 = \frac{T_S'(w_0)}{T_S''(w_0)}, \quad \tilde{\eta}_1 = b_1 w_1 \tag{35}$$

$$\eta_s = \frac{2b_s w_0}{b_{s-1}}, \; \nu_s = \frac{-b_s}{b_{s-2}}, \; \tilde{\eta}_s = \frac{2b_s w_1}{b_{s-1}}, \; \tilde{\gamma}_s = -a_{s-1}\tilde{\eta}_s, \quad s = 2, \ldots, S \tag{36}$$

$$b_0 = b_2, \quad b_1 = b_2, \quad b_s = \frac{T_s''(w_0)}{\left(T_s'(w_0)\right)^2}, \quad s = 2, \ldots, S \tag{37}$$

$$a_s = 1 - b_s T_s(w_0) \quad s = 0, \ldots, S \tag{38}$$

where ε is the damping parameter, primes denote differentiation, and

$$T_0(x) = 1 \tag{39}$$

$$T_1(x) = x \tag{40}$$

$$T_s(x) = 2xT_{s-1}(x) - T_{s-2}(x), \quad 2 \leq s \leq S. \tag{41}$$

Following [28] we set $\varepsilon = 2/13$.

S3. The reaction source terms are integrated over a full time step Δt, using as starting values the computed scalar fields at the end of the previous step. We account for half the explicit convection source terms and symbolically express the integration as:

$$(\rho Y_i)^{r+1} - (\rho Y_i)^r = \mathcal{S} \int_{\Delta t} \left[R_i + \frac{1}{2} C_i^e \right] dt \tag{42}$$

$$\rho^{r+1} - \rho^r = \mathcal{S} \int_{\Delta t} \left[R_\rho - C_{W,R} + \frac{1}{2} S_\rho^e \right] dt \tag{43}$$

$$T^{r+1} = \frac{P_0 \overline{W}^{r+1}}{\rho^{r+1}} \tag{44}$$

where R_i and $R_\rho - C_{W,R}$ are functions of the integrated state of the system (ρ, T, Y), while C_i^e and S_ρ^e are constants during the integration procedure. The integration is performed using DVODE [56], which utilizes internal time step control in order to maintain integration errors below user-specified absolute and relative tolerances $\mathcal{A}$ and $\mathcal{R}$ respectively.

S4. A convection-diffusion step identical to **S2** is performed. Specifically, the diffusion term is integrated using an S-stage RKC step of size $\Delta t/2$, which also accounts for half the convection source term. The starting values are the scalar fields computed at the end of the previous step. **S4** results in intermediate values of the scalar fields, denoted by $(\tilde{\rho}, \tilde{Y}, \tilde{T})$.

S5. Update the velocity field using the advection and diffusion terms. The convective terms are treated explicitly using AB2 over a full time step, while the viscous terms are integrated using an L-stage RKC scheme ($L \geq 2$). To this end, we define the starting values:

$$(\rho v)^0 = (\rho v)^n \tag{45}$$

and the explicit convective source term:

$$C_v^e \equiv \frac{3}{2} N^n - \frac{1}{2} N^{n-1} \tag{46}$$

Then, the convective-diffusive update takes the form:

$$(\rho v)^1 = (\rho v)^0 + \tilde{\eta}_1 \Delta t \left(F^0 + C_v^e \right) \tag{47}$$

and

$$\begin{aligned}(\rho v)^s &= (1-\eta_s-\nu_s)(\rho v)^0+\eta_s(\rho v)^{s-1}+\nu_s(\rho v)^{s-2}\\ &+ \tilde{\eta}_s\Delta t\left(F^{s-1}+C_v^e\right)+\tilde{\gamma}_s\Delta t\left(F^0+C_v^e\right)\end{aligned} \tag{48}$$

for $s=2,\ldots,L$. The coefficients of the RKC scheme are defined in a similar fashion as in **S2.** The intermediate values of density and viscosity, which are needed in the evaluation of the corresponding diffusion terms at the various stages (47–48), are obtained by interpolation between the known values at t_n and the computed predicted values at the end of **S4** [2].

The intermediate velocity field $\overline{v}\equiv v^L$ resulting from the above RKC update is then corrected using the projection step:

$$\frac{\tilde{\rho}\tilde{v}-\tilde{\rho}\overline{v}}{\Delta t}=-\nabla\tilde{p} \tag{49}$$

where $\tilde{p}$ is the solution of:

$$\nabla^2\tilde{p}=\frac{1}{\Delta t}\left[\nabla\cdot(\tilde{\rho}\overline{v})+\left.\frac{\partial\rho}{\partial t}\right|^*\right] \tag{50}$$

Here $\partial\rho/\partial t|^*$ is given by the second-order discretization [55]:

$$\left.\frac{\partial\rho}{\partial t}\right|^*=\frac{1}{2\Delta t}(3\tilde{\rho}-4\rho^n+\rho^{n-1}) \tag{51}$$

Thus, at the end of **S5**, predicted values for both scalar fields, $(\tilde{\rho},\tilde{Y},\tilde{T})$, and the velocity field, $\tilde{v}$, are available.

Non-Stiff Corrector

As mentioned earlier, the need for a corrector is dictated by the stability requirements for the variable-density projection scheme [57, 58] and not those of the scalar integration. As in [2] the corrector only affects the convective terms and is implemented as follows.

S6. Effective convection source terms for species and density evolution equations are re-evaluated using an RK2 approach based on the starting values at t_n and the predicted values from **S5**. Thus, we set:

$$C_i^* = \frac{1}{2}C_i(\tilde{\rho},\tilde{v},\tilde{Y}_i)+\frac{1}{2}C_i^n \tag{52}$$

$$S_\rho^* = \frac{1}{2}\left[C_\rho(\tilde{\rho},\tilde{v},\tilde{T})-C_{W,C}(\tilde{\rho},\tilde{v},\tilde{Y}_i)\right]+\frac{1}{2}\left(C_\rho^n-C_{W,C}^n\right) \tag{53}$$

S7. The effective non-convective change in the scalars in the predictor step is evaluated:

$$\Delta\rho \equiv \tilde{\rho}-\rho^n-\Delta t\left[\frac{3}{2}\left(C_\rho^n-C_{W,C}^n\right)-\frac{1}{2}\left(C_\rho^{n-1}-C_{W,C}^{n-1}\right)\right] \tag{54}$$

$$\Delta(\rho Y_i) \equiv \widetilde{(\rho Y_i)}-(\rho Y_i)^n-\Delta t\left[\frac{3}{2}C_i^n-\frac{1}{2}C_i^{n-1}\right] \tag{55}$$

S8. The corrected scalar fields are evaluated :

$$\rho^{n+1} = \rho^n+\Delta\rho+\Delta t\,S_\rho^* \tag{56}$$

$$(\rho Y_i)^{n+1} = (\rho Y_i)^n+\Delta(\rho Y_i)+\Delta t\,C_i^* \tag{57}$$

$$T^{n+1} = \frac{P_0\overline{W}^{n+1}}{\rho^{n+1}} \tag{58}$$

Thus, **S8** results in the fully updated scalar fields $(\rho^{n+1},Y^{n+1},T^{n+1})$.

S9. Update the velocity field using the pressure-split momentum equations. The procedure is very similar to that in **S5**, except that the intermediate scalar fields in the various RKC stages are based on interpolation between corrected scalar values at t_{n+1} and the starting values at t_n.

The velocity distribution $\hat{v} \equiv v^L$ resulting from the above RKC update is then corrected using the projection step:

$$\frac{\rho^{n+1}v^{n+1} - \rho^{n+1}\hat{v}}{\Delta t} = -\nabla\hat{p} \tag{59}$$

where $\hat{p}$ is the solution of:

$$\nabla^2\hat{p} = \frac{1}{\Delta t}\left[\nabla\cdot(\rho^{n+1}\hat{v}) + \left.\frac{\partial\rho}{\partial t}\right|^{**}\right] \tag{60}$$

with the density gradient approximated from:

$$\left.\frac{\partial\rho}{\partial t}\right|^{**} = \frac{1}{2\Delta t}(3\rho^{n+1} - 4\rho^n - \rho^{n-1}) \tag{61}$$

This completes the integration cycle, as updated values for the scalar fields, ρ^{n+1}, Y^{n+1}, and T^{n+1}, and the velocity field, v^{n+1}, are available.

Remarks

1. *RKC Stability:* As discussed earlier, one of the advantages of using extended stability schemes is that they provide an effective means for minimizing the number of source term evaluations. The present single-step, S-stage, second-order RKC method has a real stability limit $\beta(S)$ given by [21]:

$$\beta(S) \simeq \frac{2}{3}\left(S^2 - 1\right)\left(1 - \frac{2}{15}\varepsilon\right) \tag{62}$$

   where ε is the damping parameter (see Eqs. 35–41). For the selected value $\varepsilon = 2/13$ we have $\beta(S) \simeq 0.65(S^2 - 1)$. Given a global integration time step, which for the present operator-split construction is selected based on accuracy considerations [2], Eq. (62) is used to determine the minimum number of stages S needed to guarantee internal stability of the RKC integration. This situation should be contrasted with the approach adopted in our previous effort [2], where the treatment of the diffusion term is based on repeated application of an explicit multistep scheme. In [2], we had relied on a second-order Adams-Bashforth scheme (AB2), whose real stability limit is 1 ($\lambda_v\Delta t < 1$ for stability, where $\lambda_v = 2^{n+1}\alpha/\Delta x^2$, and where n is the number of spatial dimensions). It follows that the ratio of the number of source term evaluations in the RKC method to the corresponding number in the approach based on repeated fractional AB2 updates is approximately $S/\beta(S)$. Since β increases quadratically with the number of stages S, one would expect RKC to exhibit a significant speed up, of the order of $\beta(S)/S$, as S increases.

2. *Extrapolated Transport Properties:* As discussed in section 1, with detailed transport models the CPU cost of the numerical integration of diffusion is dominated by the evaluation of the mixture-averaged transport properties. Specifically, the cost of evaluating these properties is significantly larger than that associated with the evaluation of diffusion fluxes, the divergence of these fluxes, and the numerical integration used to update the corresponding fields. This suggests that further speedup of the computations can be achieved if one could minimize the number of direct transport property evaluations. In the present work, we explore an internal extrapolation scheme that is based on (i) directly evaluating the transport properties at the beginning of the integration step, and (ii) using stored values obtained at the beginning of the previous time step in order to estimate the values required at the various internal RKC stages –or in the case of the original construction [2] at the various internal fractional steps.

   We briefly outline this extrapolation procedure for the case of a generic transport parameter ζ. Let ζ^n and ζ^{n-1} denote the (directly-evaluated) values of ζ at t_n and t_{n-1}, respectively. In both the RKC approach and the repeated-AB2 scheme from [2], we need estimates (ζ^s) for the transport properties

at intermediate times, t_s, with $t_n \leq t_s < t_{n+1}$. In the RKC approach, for instance, these intermediate estimates are needed to evaluate the diffusion fluxes D_ρ^s and D_i^s appearing in Eqs.(32–33). In the computations, the linear extrapolation procedure:

$$\zeta^s = \zeta^n + \frac{t_s - t_n}{\Delta t}\left(\zeta^n - \zeta^{n-1}\right) \tag{63}$$

is used to determine these estimates. Note that with this approach the overall second-order convergence of the time integration procedure is formally maintained, and actually achieved in the computations as discussed below.

We have remarked earlier that using RKC integration one would expect a speedup factor of the order $\beta(S)/S$ with respect to our previous split construction in [2]. We also noted that for the mixture-averaged transport model, the direct evaluation of diffusion source terms is dominated by the calculation of transport properties. These two observations suggest that combined, the RKC integration and the extrapolation procedure would lead to speedups of the order of $\beta(S)$ over our previous scheme [2]. The computational tests of the following section reveal that the additional enhancement due to the extrapolation procedure is in fact achieved.

3. *Coarse Jacobian:* In addition to the above extrapolation procedure, we have briefly explored an efficiency enhancement approach that is based on the utilization of chemical-source-term Jacobian data which are (pre-) evaluated on a coarse computational grid. This development is motivated by the observation that in most premixed combustion applications the flame region accounts for a small fraction of the computational domain, which essentially consists of regions corresponding to either cold reactants or burnt products. In these regions, there are weak variations in the chemical composition of the mixture, which suggests that the Jacobian data used in the stiff integration of the chemical source term can be approximated using neighboring point values. Additional motivation for this approach comes from the observation [2] that in the burnt and unburnt regions, the stiff integration of the chemical source term generally requires 2-3 function evaluations and a single Jacobian evaluation only.

   In the computations, we implement a simple Jacobian extrapolation scheme by first defining a coarse computational grid. The coarsening is specified in terms of the grid ratio P which corresponds to the ratio of fine to coarse grid cells in each coordinate direction. The coarsening is implemented in such a way that a coarse computational cell (in 2D) corresponds exactly to P^2 cells of the original fine mesh. Prior to the stiff integration procedure, a test is performed in order to determine the coarse grid cells in which the temperature fluctuations are small. The test checks whether the peak temperature difference, ΔT_{max}, between the four corners of the coarse cell, falls below a user-prescribed threshold, ΔT_o. When this simplified criterion is satisfied, i.e. $\Delta T_{max} < \Delta T_o$, the Jacobian is evaluated at or near the center of the coarse cell and then propagated to the fine grid cells that are contained within the coarse cell. This coarse-grid estimate is then supplied as an initial, approximate, Jacobian in the stiff DVODE integration at the corresponding fine cells. If, within the DVODE integration, an updated Jacobian is needed, the procedure automatically reverts to direct evaluation of the Jacobian, which is based on exact expressions obtained by analytically differentiating the chemical source term. On the other hand, when the above simplified criterion is not satisfied, the direct evaluation procedure is used whenever the Jacobian is needed, as performed in the previous constructions [1, 2].

   Note that since the coarse Jacobian is used as an initial guess only, and since the integration reverts back to the direct evaluation procedure when a more accurate Jacobian is needed, the present approach is not expected to have a major impact on the behavior of the DVODE integration [56]. Furthermore, since DVODE implements an error-control scheme that does not involve the Jacobian, minimal effect on the numerical results is also expected. Thus, the present coarse-Jacobian procedure offers the possibility of reducing the CPU cost of the stiff integration, with essentially no impact on its numerical properties. The behavior of the coarse Jacobian option is briefly explored in 2D tests described below.

3 Results and Discussion

The order of convergence, accuracy, and efficiency of the overall numerical construction using RKC, transport property extrapolation, and coarse-Jacobian, are studied using an analytically solvable one-dimensional (1D) reacting front problem as well as 1D/2D premixed flame problems using detailed kinetics and transport.

3.1 Simplified 1D Analysis

In order to test the performance of the RKC integration in the split-stiff scheme, we repeat part of the simplified 1D analysis originally introduced in [2]. This analysis is based on the following family of reaction-diffusion equations:

$$\frac{\partial u}{\partial t} = \frac{\partial^2 u}{\partial x^2} + \frac{8}{\delta^2} u^2 (1-u), \quad -\infty \leq x \leq \infty, \tag{64}$$

with boundary conditions $u(x) \to 1$ as $x \to -\infty$ and $u(x) \to 0$ as $x \to \infty$. Here, $\delta > 0$ is a freely selected parameter. The exact solution of the above system is given by:

$$u(x,t) = \frac{1}{2}\left(1 - \tanh\left[\frac{x-ct}{\delta}\right]\right) \tag{65}$$

where $c = 2/\delta$. Thus, the solution (65) corresponds to a steady-propagating front of width δ and speed c. The system is briefly used below to analyze the behavior the splitting errors in the present scheme, and the experiences are contrasted with the results of the detailed analysis given in [2].

To this end, the numerical scheme outlined above is adapted to the solution of equation (64). The simulations are initialized using the steady solutions given in equation (65), i.e. we set:

$$u(x,0) = \frac{1}{2}\left(1 - \tanh\left[\frac{x}{\delta}\right]\right) \tag{66}$$

Solutions are obtained using a finite difference grid which extends over the interval $-Z \leq x \leq Z$, $Z \gg \delta$. Second-order centered differences are used to discretize the diffusion term. At $x = -Z$, the Dirichlet condition $u(-Z,t) = 1$ is used, while a homogeneous Neumann condition is used at $x = Z$. The domain truncation length Z is selected large enough so that the solution is essentially independent of both Z and the conditions imposed at the boundaries of the domain.

The numerical tests below focus on a propagating front with $\delta = 1$. Simulations are performed on a finite domain with $Z = 20$, with different resolution levels $\Delta x = 2Z/N$, where N is the total number of sub-intervals. Equation (64) is integrated to $t = 0.6144$, such that the front propagates for a distance approximately 1.2 times its own width. At the end of the computations, local errors are computed using the exact solution,

$$e_i^n = u_i^n - u_{\text{ex}}(x_i, t_n) = u_i^n - \frac{1}{2}\left(1 - \tanh\left[\frac{x_i - 2t_n/\delta}{\delta}\right]\right) \tag{67}$$

and a global error measure is formed using the discrete l_2 norm,

$$E_2 = \left[\frac{1}{N+1}\sum_{i=1}^{N+1}\left(u_i^n - u_{\text{ex}}(x_i,t_n)\right)^2\right]^{1/2}. \tag{68}$$

The error analysis is based on numerical solutions obtained on three different grid levels, with $N = 1000$, 2000, and 4000. At each grid resolution, simulations are performed using the symmetrically-split RKC-stiff scheme with different values of the global time step Δt. The integration is based on first integrating the diffusion term over a half-time step using an S-stage RKC scheme, updating the reaction term over Δt using DVODE, and then performing a second S-stage RKC update of the diffusion term over $\Delta t/2$. The number of stages S is varied, and the results are interpreted using the total number, $M = 2S$, of RKC stages during the full time step.

Figure 1 shows the spatial distribution of the error at the end of the computations for three resolution levels, $N = 1000$, 2000 and 4000, and different values of M. The diffusion half-step corresponds to the RKC

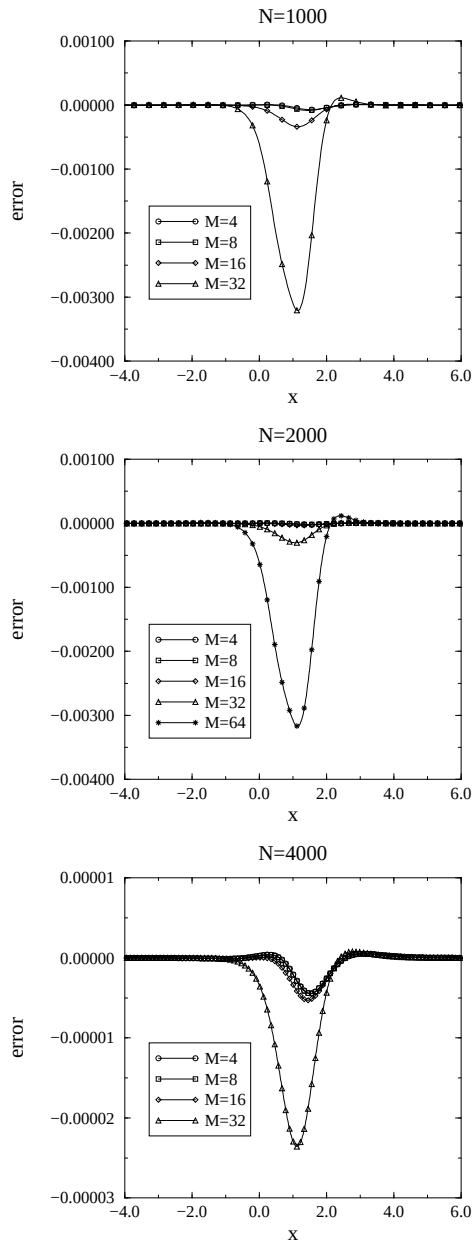

Figure 1: Spatial distribution of the error between the numerical and exact solutions for the split scheme with different values of M. The absolute and relative tolerances used are 10^{-13} and 0, respectively. The computations are performed with $\delta = 1$, $Z = 20$, and $N = 1000$ (top), $N = 2000$ (middle), and $N = 4000$ (bottom). The time step in the fractional diffusion steps corresponds to the RKC critical stability limit.

$N = 1000$, $\Delta x = 0.04$

Scheme	$\Delta t \times 10^3$	RMS Error $\times 10^5$	Order of Convergence
Split/RKC, $M = 4$	1.555	1.0039	1.9994
Split/RKC, $M = 8$	7.679	1.1991	2.0013
Split/RKC, $M = 16$	30.72	5.0911	2.0034
Split/RKC, $M = 32$	102.4	49.391	2.0061

$N = 2000$, $\Delta x = 0.02$

Scheme	$\Delta t \times 10^4$	RMS Error $\times 10^6$	Order of Convergence
Split/RKC, $M = 4$	3.898	2.4927	1.9201
Split/RKC, $M = 8$	19.44	2.6097	1.9994
Split/RKC, $M = 16$	80.84	5.0125	2.0010
Split/RKC, $M = 32$	307.2	45.304	2.0031
Split/RKC, $M = 64$	1024.	488.61	1.9999

$N = 4000$, $\Delta x = 0.01$

Scheme	$\Delta t \times 10^4$	RMS Error $\times 10^6$	Order of Convergence
Split/RKC, $M = 4$	0.9748	0.62193	0.1532
Split/RKC, $M = 8$	4.872	0.62929	1.9593
Split/RKC, $M = 16$	20.41	0.76214	1.9994
Split/RKC, $M = 32$	81.92	3.53194	2.0009

Table 1: Root-mean-square error and order of convergence for reacting front simulations with $\delta = 1$ and $Z = 20$. The split scheme uses an absolute tolerance of 10^{-13}.

Scheme	Δt_c	$\Delta t_c/2$	$\Delta t_c/4$
Split/RKC, $M = 4$	6.21931×10^{-7}	6.21437×10^{-7}	6.20972×10^{-7}
Split/RKC, $M = 8$	6.29295×10^{-7}	6.23576×10^{-7}	6.22080×10^{-7}
Split/RKC, $M = 16$	7.62144×10^{-7}	6.65435×10^{-7}	6.29704×10^{-7}
Split/RKC, $M = 32$	3.53194×10^{-6}	1.26834×10^{-6}	7.61925×10^{-7}

Table 2: Root mean square errors for reacting front simulations with $\delta = 1$, $Z = 20$, and $N = 4000$. The split calculations use an absolute tolerance of 10^{-13}.

stability limit (Eq. 62), so that the global time step is given by $\Delta t = \Delta t_c \equiv 0.65(S^2-1)\Delta x^2/2$. Here, Δt_c denotes the *global* critical time step. The stiff integration of the reaction term uses zero relative tolerance and an absolute tolerance of 10^{-13}. For the cases of Fig. 1, Table 1 shows the corresponding RMS errors, together with the temporal order of convergence of the calculations. The latter is obtained by repeating the calculations with decreasing time steps and monitoring the differences between numerical solutions obtained at the same spatial resolution level. This enables us to isolate time discretization errors and determine the temporal order of convergence.

Figure 1 and Table 1 show that when M is small the spatial error distribution and the RMS values are essentially independent of the value of M. For $N = 4000$, the errors are essentially constant when $M \leq 16$, while for $N = 1000$ and 2000 errors are nearly constant when $M \leq 8$. Meanwhile, Table 2 shows that with $N = 4000$, the RMS error at the final time is essentially independent of the time step, except with $M = 32$ at largest value of Δt. The results are consistent with our earlier experiences in [2] and lead to the same conclusions. Specifically, as long as the global time step is below a well defined threshold, the RMS errors at the final time are dominated by spatial errors and are independent of both M and Δt. (See detailed discussion in [2].). For the present example, this threshold is about 20×10^{-4}, independent of the spatial resolution level.

It is instructive to compare the present RMS-error predictions with those obtained in our earlier analysis [2], in which the diffusion half-step was treated with repeated RK2/AB2 fractional steps. The comparison

shows that the time-step level at which splitting errors become significant is essentially the same in both approaches. When the global time step is below the above threshold, the RMS errors obtained using the present scheme and the previous scheme are nearly identical. This is not surprising since, as remarked earlier, spatial errors are dominant at "small" Δt and since the same spatial discretization approximation is used in both methods. However, the comparison also shows that there is close agreement in the RMS errors at larger values of Δt. This close correspondance indicates that at a given (large) value of Δt the *splitting errors* in both schemes behave in essentially the same fashion, independently of the number of fractional steps or RKC stages. This allows us to immediately exploit the results and conclusions of the previous analysis [2], and in particular allows us to avoid repeating the detailed study of the order of convergence and the effect of user-defined tolerances in the stiff integration procedure.

We conclude this study by noting that Table 1 also indicates that the split, stiff-RKC, time integration scheme does achieve second-order convergence. Second-order convergence is in fact observed in all cases considered, except for $N = 4000$ with $M = 4$. As discussed in [2], this apparent drop in the computed convergence rate can be traced to fact that at small Δt the integration errors can become comparable to the selected tolerances in the stiff integration.

3.2 Flame with Detailed Kinetics and Transport

We consider a premixed methane-air flame at atmospheric pressure, burning into a stoichiometric 20% N_2-diluted mixture at room temperature. We use the GRImech1.2 [22] mechanism, which includes both C_1 and C_2 molecules, and involves 32 species and 177 reactions. We also use the above outlined DRFM mixture-averaged transport model, with extrapolation of transport properties. We examine the convergence of the scheme in 1D, and examine its efficiency in 2D.

3.2.1 One-Dimensional Flame

The second-order convergence rate of the scheme is illustrated in Figure 2. The plots are based on analysis of the computed flame solutions obtained with successive time-step refinement using the present scheme and the non-split semi-implicit scheme which uses the same stiff ODE integration procedure as outlined in [1]. The self convergence results are based in the RMS error between computed flame solutions with the present scheme with successive time-step refinement. The cross-convergence results are based on the RMS error between the computed flame solutions using the present scheme and the non-split scheme. The spatial discretization is held fixed. The two schemes use the same stiff-integrator tolerances with absolute tolerance $\mathcal{A} = 10^{-14}$ and relative tolerance $\mathcal{R} = 10^{-8}$. The RKC scheme uses $M = 2S = 16$, $L = 4$. The two figures illustrate the second-order self and cross-convergence of the RKC scheme using the temperature, velocity, and CH, HCO mole fraction fields.

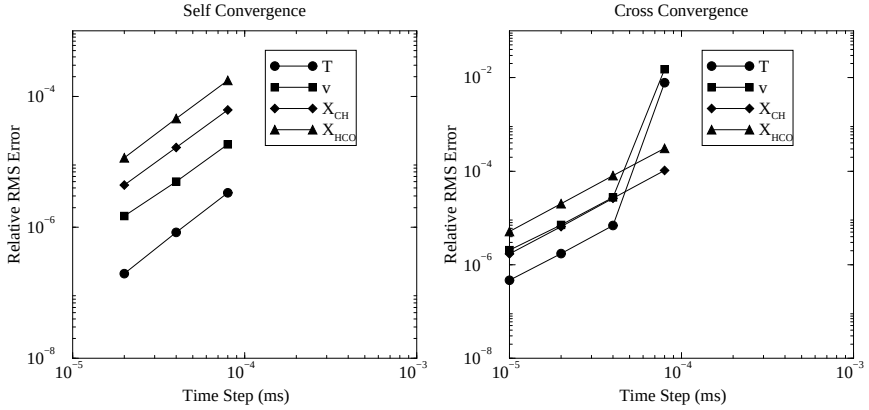

Figure 2: Second-order self and cross-convergence with respect to Δt in 1D. Self convergence is for an operator-split RKC case with $M = 16$, $L = 4$, $\mathcal{R} = 10^{-8}$, $\mathcal{A} = 10^{-14}$ and with extrapolation of transport properties. The cross convergence data compares this case to a case with no operator splitting, same ODE integrator tolerances, and without extrapolation of transport properties.

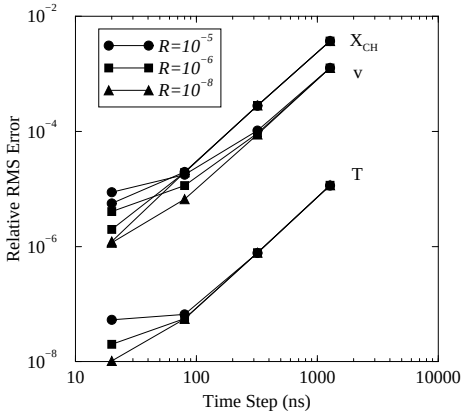

Figure 3: Variation in relative RMS error in temperature, velocity, and CH mole fraction in a 1D flame, with changes in the number of RKC stages, starting with $M = 4$ and $L = 2$ ($\Delta t = 20$ ns), and increasing by factors of 2 to $M = 32$ and $L = 16$ ($\Delta t = 1280$ ns). The x-axis shows the global time step (Δt) size, which varies with M, L. Plots are shown for three levels of ODE integrator tolerances ($\mathcal{A} = \mathcal{R} = R$), showing the expected degradation in error reduction and the second-order convergence rate as the explicit time integration error becomes on the order of the implicit ODE integrator error (governed by the specified tolerances).

We also examine the dependence of RMS error between the split and non-split schemes on the number of RKC stages, allowing the time step to vary with the square of the number of stages, in accordance with the growth of the stability boundary on the negative real axis. The results are shown in Figure 3, where second-order growth with time-step is again observed, over the range $M = 4-32$, $L = 2-16$, for three selected error tolerances. As observed in [2], the low-Δt minimum error plateau reached is dictated by the error threshold implemented in the stiff integration procedure. In contrast with [2], however, the stabilized characteristic of the RKC construction allows the efficient utilization of very large time steps, such that time discretization/splitting errors become comparable to spatial discretization errors, as shown in Figure 4 at the high time-step limit. Note that the largest practical time steps used in [2], were well below the level where time-splitting errors become large compared to spatial discretization truncation errors. In the present context, using a time-step above 1 μs will lead to the dominance of time-integration errors over those of spatial discretization.

3.2.2 Two-Dimensional Flame-Vortex-Pair Interaction

We finally examine the utility of the present construction in the context of a 2D computation of the interaction of the above premixed methane-air flame with a counter-rotating vortex-pair in the reactants stream. The evolution of the flame HCO mole fraction and vorticity fields are shown in Figure 5 over a time span which includes substantial stretch and contortion of the flame, reduction in burning rate and radical concentrations in the flame, and the production of baroclinic vorticity dipoles. Performance tests were conducted on a 32-processor 195Mhz Silicon Graphics ORIGIN2000 machine, with no other significant user processes running. They involved a 256×1024 mesh, with $M = 16$, $L = 4$, $\mathcal{A} = \mathcal{R} = 10^{-6}$, and $\Delta t = 200-700$ ns. The CPU timing results, showing the time spent per processor per time step, are shown in Table 3 for a number of cases of operating conditions. The Coarse-Jac case refers to the utilization of Jacobian evaluations interpolated from a coarse mesh as outlined above, while the no-Coarse-Jac refers to the full (analytical) evaluation of Jacobians at each mesh cell.

We note first that, for RKC with mixture-averaged transport and no-Coarse-Jac, the overall speedup in going from $\Delta t = 200$ to 700 ns is about a factor of 3, despite the relatively small increase in CPU-time per time step (43.7 to 53.5, or 193.9 to 203.1). Moreover, again for RKC with mixture-averaged transport and $\Delta t = 700$ ns, the CPU-time savings in using the coarse Jacobian are about 10% when transport properties are extrapolated. This advantage is almost completely lost when no extrapolation is used because of the dominance of the diffusion integration costs over the stiff-integration cost in this case, as evidenced by the increase by a factor of 4 of the CPU-time (e.g. from 49.2 to 199.7) when no extrapolation is used. In fact, with RKC and mixture-averaged transport, using extrapolation of transport properties leads to a speedup of 3.8 to

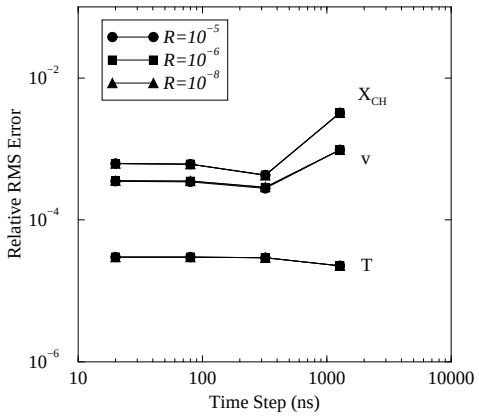

Figure 4: Variation in relative RMS error, including spatial truncation errors, comparing the temperature, velocity, and CH mole fraction in a 1D flame, with changes in the number of RKC stages for the case with $N = 512$ versus the non-split case with $N = 2048$. The number of RKC stages starts with $M = 4$ and $L = 2$ ($\Delta t = 20$ ns), and increases by factors of 2 to $M = 32$ and $L = 16$ ($\Delta t = 1280$ ns). The x-axis shows the global time step (Δt) size, which varies with M, L. Plots are shown for three levels of ODE integrator tolerances $\mathcal{A} = \mathcal{R} = R = 10^{-5}$, 10^{-6}, and 10^{-8}. This is little change in the errors with Δt at time step sizes below about 100 ns, due to the dominance of spatial errors. As Δt approaches 1 μs, the temporal errors become significant compared to the spatial errors.

4.4 depending on the time step and the utilization of the coarse-Jacobian. This large speedup is a reflection of the high cost of the mixture-averaged transport property evaluations. The table lists the total CPU-time costs ensuing from the temperature-tabulated transport property evaluation used in our earlier work [1, 2] versus the present mixture-averaged formulation both for RKC and the previous RK2/AB2 implementations, giving a factor of 6 increase in total CPU-time in both cases, clearly justifying the need for the present transport property extrapolation procedure. The combination of RKC, Extrapolation, and Coarse-Jac at $\Delta t = 700$ ns, versus RK2/AB2, no-Extrapolation, no-Coarse-Jac at 200 ns, both using mixture-averaged transport, gives an overall speedup factor of 15 [=(214.0/49.2)(700/200)].

Another important factor in code speedup pertains to the efficient utilization of cache-memory architecture of the computational hardware. In the present context, minimization of cache-memory overheads were pursued on two fronts. To begin with, CPU/memory-intensive functions were recoded using a high-level meta-code that parses hand-coded Fortran subroutines and produces substitute auto-code. The auto-code routines involve completely unrolled loops and hardwired loop index variables and array references. This approach

Mixture-averaged transport

	no-Coarse-Jac		Coarse-Jac
Transport	$\Delta t = 200$ ns	$\Delta t = 700$ ns	
Extrapolation	43.7	53.5	49.2
no-Extrapolation	193.9	203.1	199.7

no-Extrapolation, no-Coarse-Jac, $\Delta t = 200$ ns

Transport	RKC	RK2/AB2
Mixture-averaged	193.9	214.0
Temperature-tabulated	31.4	35.1

Table 3: CPU times (sec/proc/time-step) for a 2D flame-vortex-pair interaction on a 256×1024 mesh, with $M = 16$, $L = 4$, on a 32-processor 195Mhz SGI ORIGIN2000.

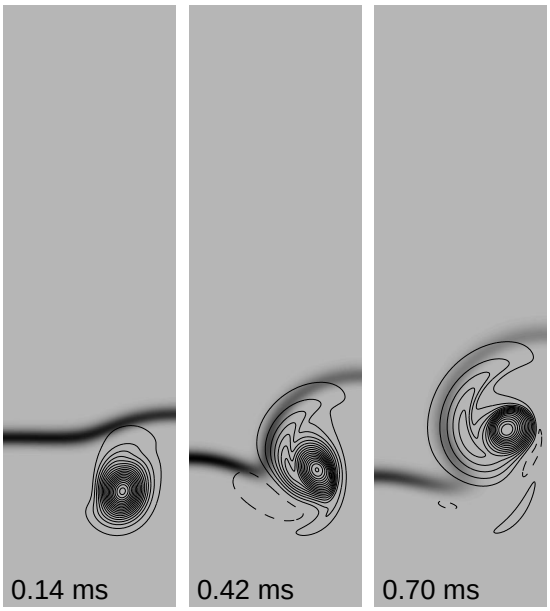

Figure 5: Two-dimensional flow-flame evolution showing contours of vorticity superposed on a gray-scale representation of the HCO mole fraction field.

was used for the chemical source terms function and jacobian evaluation routines as in [1, 2]. Secondly, data structures were tailored to the effective utilization pattern in the code. Specifically, given the large number of species to be accessed at each spatial location, arrays were structured to allow the inner-most index to refer to species identity, thereby storing species information at a given mesh cell in a contiguous memory segment. This last approach lead to a doubling of parallel code execution speed when running on a relatively large number of processors (30-40).

We note finally that, while two-dimensional flame computations are too expensive for use in a convergence study, we have examined the RMS differences between 2D flame-vortex computations for a select set of conditions at a time of 0.7 ms (vis. Fig. 5). We evaluate the maximum and RMS relative differences between computed flow solutions at this time instant with regard to the effect of (1) extrapolation of transport properties, and (2) increased time step. We find that, in general, RMS relative differences ($\|\phi_a - \phi_b\|_2 / \|\phi_a\|_\infty$) of all flow variables are about an order of magnitude smaller than the maximum relative differences ($\|\phi_a - \phi_b\|_\infty / \|\phi_a\|_\infty$). This is because the flame region, where field variable gradients and discretization errors are significant, is a small fraction of the overall computational domain. Thus, in order to examine the errors in the high-gradient regions, we focus on the ∞-error norm. The use of extrapolation of transport properties is found to have little consequence on the computed results, with a maximum relative difference in field variables ranging from 0.0005% to 0.01%. Larger maximum differences, ranging from 0.2% to 5%, are observed due to the increased time step (from 200 to 700 ns) with the RKC scheme. Given the speed of the vortex in Fig. 5, and the consequent convective CFL number of 0.34, further increases in the time step, while feasible within RKC, are not advisable for accuracy considerations.

Conclusions

We have presented an operator-split scheme for reacting flow modelling using an optimal combination of implicit integration of stiff chemical source terms and explicit integration of diffusion terms. Integration of the chemical terms uses an implementation of the DVODE ODE integration package, while the diffusion integration uses a Runge-Kutta-Chebyshev scheme, a specific implementation of stabilized Runge-Kutta schemes with extended stability along the negative real axis.

We also presented an approach for efficient utilization of detailed transport models in the context of multi-stage diffusion integration, where transport properties are evaluated once per time step and then extrapolated to the internal stages. This approach is crucial for the utilization of detailed transport in operator-split or multi-stage integration constructions. Detailed transport is impractical in this context if properties were evaluated at each RK-stage, as the resulting exorbitant cost of the diffusion computation significantly diminishes the advantage of operator-splitting.

We also outlined and demonstrated an approach for efficient utilization of approximate jacobians in the context of stiff integration of multidimensional reacting flow. Given the significant cost associated with jacobian evaluations, the use of pre-evaluated neighbor values in regions of low spatial gradients provides for significant savings at no cost to accuracy or stability.

This construction was implemented in the context of a projection scheme solution of the low-Mach number reacting flow equations, with detailed chemical kinetics and transport. We used a mixture-averaged transport formulation based on a recently developed transport-property model that offers significant improvements in accuracy relative to earlier work.

We examined and analyzed errors and convergence rates of the overall construction using both analytical 1D reaction-fronts and a methane-air flame in 1D and 2D. We demonstrated second-order convergence, and outlined the interaction of time-integration and spatial errors, and the role of stiff integrator tolerances. The efficient stabilized construction of the RKC scheme allowed the stable use of large time steps. In fact, the scheme allows stable integration with time steps that are so large as to result in the dominance of time-integration errors over spatial errors. As with implicit schemes, prudent choice of the time step is necessary to maintain a desired degree of accuracy, a situation that is typically not encountered in explicit integrators due to the limitation on time step size by stability constraints.

Finally, we also demonstrated the speedup and efficiency of the construction in 2D methane-air reacting flow. Given the increased time step advantages of RKC, the efficient extrapolation of transport properties, and the coarse jacobian implementation, an overall speedup factor of 15 is observed without a substantial impact on the accuracy of the computations.

Acknowledgements

Support was provided by the US Dept. of Energy (DOE), Office of Science, Office of Basic Energy Sciences (BES), Division of Chemical Sciences, Geosciences, and Biosciences. Computations were performed at Sandia National Laboratories and at the National Center for Supercomputer Applications.

Appendix

The quantity $Pi(T) = \lambda_i/\lambda_i^{(m)}$, often termed the Eucken ratio, represents the pure species thermal conductivity as normalized by the translational component of that conductivity. For atomic species the Eucken ratio is by definition unity, while it is greater than unity for molecular species. Various models for the Eucken ratio have been proposed, but these have achieved only limited success in predicting experimentally observed behavior, particularly for species that are polar (e.g. H_2O or HCN) or species with multiple coupled internal modes that are excited at moderate temperatures (e.g. C_2H_2 or C_2H_4). Applying the model proposed by Wakeham and co-workers (see for example [59]) as based on the set of cross-sections developed by Thijsse *et al.* [60]

we write

$$P_i(T) = \frac{\left(\frac{2}{5}\frac{c_{p,i}}{R}\right)^2}{\left[1+\left(\frac{2}{5}\frac{c_{p,i}}{R}-1\right)\frac{5(1+F_i)}{4A_i^*}\right]} \tag{A1}$$

where $A_i^* \equiv \Omega_{ii}^{(22)^*}$, c_p is the specific heat and R is the gas constant. Here

$$F_i(T) = \Delta_i + \frac{16A_i^*}{15\pi Zr_i} \tag{A2}$$

where $\Delta_i(T)$ is a resonance correction and $Zr_i(T)$ is the rotational collision number.

The formulation used in CHEMKIN [47] and in EGLIB [61] can be recovered by expanding Eq. (A1) in the limit of F much less than unity (i.e. the combined limits of Δ_i much less than and Zr_i much greater than unity). For almost all of the species of interest here, however, these limits are poorly satisfied. Taking H_2O as an example, $F \approx 1.2$ at 300K falling to $F \approx 0.25$ at 3000K. For H_2O, experimental data gives values of $P \approx 1.2$ rising to 2.15 at 3000K. The model employed in CHEMKIN yields values of $P \approx 1.6$ at 300K rising to 2.45 at 3000K (a systematic overprediction of order 30% at low temperatures to 14% at high temperatures). On the other hand, the model of Eqs. (A1) and (A2) matches the experimental data to within a few percent over the full temperature range of interest. Similar results (i.e. noticeable systematic errors using the model employed in CHEMKIN and good agreement using the model of Eq. (A1)) were found for a large collection of polar species (including HCN and HF that are a particular challenge owing to a combination of relatively small size and large dipole moment) as well as coupled mode species (e.g. C_2H_2 and C_2H_4) and for H_2.

Where available, experimental data was used to obtain values for $P_i(T)$. The model of Eqs. (A1) and (A2) was used to extend these data to higher temperatures and to estimate $P_i(T)$ for species where no transport data exists. The resonance correction Δ_i was evaluated using the relations proposed by Mason and Monchick [62]. The additional molecular properties required (rotational constants for the molecules) were obtained from the spectroscopic literature, and specific heats were obtained from the CHEMKIN thermodynamic data base. A variety of models have been proposed for the rotational collision number, however these have met with limited success in predicting experimental data. We have adopted the temperature-independent model of Brout [63]. Where experimental thermal conductivity and viscosity data are available at lower temperatures, the value of Zr was extracted using Eqs. (A1,A2) and this was used to predict the value of $P_i(T)$ at higher temperatures. Where no experimental data exists, Zr was fixed to a value of 2. This particular value is a reasonable compromise of existing experimental data and does not appear to degrade prediction in comparison to the uncertainties in the experimental data.

To predict the purely translational transport properties (e.g. viscosity, binary diffusivity, thermal diffusivity) the DRFM model requires eight molecular parameters for each pure species. These are the Lennard-Jones potential radius and energy, Born-Mayer potential radius and energy, molecular weight, dipole moment, polarizability and dispersion energy. Details on the DRFM model and a limited database are given by Paul [23]. For the results presented here, a complete database has been newly assembled for all of the species in the simulation. This database was obtained by using the DRFM model to extract parameters from available transport properties or from other experimental data (e.g. beam and spectroscopic data). Little or no transport data exists for the radical molecular species. In these cases the database was created using models from the literature and more primitive molecular properties, as outlined by Paul [23]. This procedure was validated by testing against all of the species with known properties. A full compilation of this database will be the subject of a future report.

It is noteworthy that on-line evaluation of translational transport properties from a molecular potential model is the most efficient and compact approach. The model for $P_i(T)$ requires up to seven additional molecular parameters, temperature-dependent specific heats, and evaluation of somewhat complex models for $\Delta(T)$ and $Zr(T)$. It is more compact and efficient to evaluate $P_i(T)$ off-line to be used in the simulation in the form of a polynomial representation for each pure species. This overall strategy preserves the capacity to introduce second-order corrections and second-order properties as well as higher order mixture-averaged or multicomponent transport properties.

References

[1] Najm, H.N., Wyckoff, P.S., and Knio, O.M., *J. Comp. Phys.*, 143(2):381–402 (1998).

[2] Knio, O.M., Najm, H.N., and Wyckoff, P.S., *J. Comp. Phys.*, 154:428–467 (1999).

[3] Courant, R., Friedrichs, K.O., and Lewy, H., *Mathematische Annalen*, 100:32–74 (1928) (Translated to: On the Partial Difference Equations of Mathematical Physics, IBM J. Res. Dev., vol. 11, pp. 215-234, 1967).

[4] Anderson, D.A., Tannehill, J.C., and Pletcher, R.H., *Computational Fluid Mechanics and Heat Transfer*, Hemisphere Pub. Co., New York, (1984).

[5] Najm, H.N., Knio, O.M., Paul, P.H., and Wyckoff, P.S., *Comb. Sci. Tech.*, 140(1-6):369–403 (1998).

[6] Hundsdorfer, W.H., Report NM-N9603, CWI, Amsterdam, (1996) http://info4u.cwi.nl.

[7] Spee, E.J., in *Air Pollution III* (H. P. *et al.*, Ed., volume 1, Comput. Mech. Publ., Southampton-Boston, (1995), pp. 319–326, .

[8] Verwer, J.G., Blom, J.G., van Loon, M., and Spee, E.J., *Atmos. Eviron.*, 30:49–58 (1995).

[9] Hundsdorfer, W., and Verwer, J.G., *App. Num. Math.*, 18:191–199 (1995).

[10] Spee, E.J., de Zeeuw, P.M., Verwer, J.G., Blom, J.G., and Hundsdorfer, W.H., Report NM-R9620, CWI, Amsterdam, (1996) http://info4u.cwi.nl.

[11] Verwer, J.G., Spee, E.J., Blom, J.G., and Hundsdorfer, W.H., *SIAM J. Sci. Comput.*, 20:1456–1480 (1999) in press.

[12] Spee, E.J., Verwer, J.G., de Zeeuw, P.M., Blom, J.G., and Hundsdorfer, W., *Mathematics and Computers in Simulation*, 48:177–204 (1998).

[13] Khan, L.A., and Liu, P.L.-F., *Comput. Methods Appl. Mech. Engrg.*, 127:181–201 (1995).

[14] Strang, G., *SIAM J. Numer. Anal.*, 5(3):506–517 (1968).

[15] Burstein, S.Z., and Mirin, A.A., *J. Comp. Phys.*, 5:547–571 (1970).

[16] Yoshida, H., *Physics Letters A*, 150(5,6,7):262–268 (1990).

[17] Sheng, Q., *IMA J. Numer. Anal.*, 9:199–212 (1989).

[18] Wright, J.P., *J. Comp. Phys.*, 140:421–431 (1998).

[19] Day, M.S., and Bell, J.B., *Combust. Theory Modelling*, 4:535–556 (2000).

[20] Kee, R.J., Rupley, F.M., and Miller, J.A., Sandia Report SAND89-8009B, Sandia National Labs., Livermore, CA, (1993).

[21] Verwer, J.G., *App. Num. Math.*, 22:359–379 (1996).

[22] Frenklach, M., Wang, H., Goldenberg, M., Smith, G.P., Golden, D.M., Bowman, C.T., Hanson, R.K., Gardiner, W.C., and Lissianski, V., Top. Rep. GRI-95/0058, GRI, (1995).

[23] Paul, Phillip H., Sandia Report SAND98-8203, Sandia National Laboratories, Albuquerque, New Mexico, (1997).

[24] Paul, P., and Warnatz, J., *Twenty-Seventh Symposium (International) on Combustion*, The Combustion Institute, pp. 495–504, (1998).

[25] van der Houwen, P.J., and Sommeijer, B.P., *ZAMM*, 60:479–485 (1980).

[26] Verwer, J.G., *ZAMM*, 62:561–563 (1982).

[27] Verwer, J.G., Hundsdorfer, W.H., and Sommeijer, B.P., *Numer. Math.*, 57:157–178 (1990).

[28] Sommeijer, B.P., Shampine, L.F., and Verwer, J.G., *J. Comput. Appl. Math.*, 88:315–326 (1997).

[29] van der Houwen, P.J., *Numer. Math.*, 20:149–164 (1972).

[30] van der Houwen, P.J., *Construction of integration formulas for initial value problems*, North-Holland, Amsterdam-New York, (1977).

[31] Verwer, J.G., *J. Comp. App. Math.*, 3(3):155–166 (1977).

[32] Verwer, J.G., *ACM Transactions on Mathematical Software*, 6(2):188–205 (1980).

[33] Medovikov, A.A., in *Numerical Analysis and Its Applications* (L. Vulkov J. Waśniewski and P. Yalamov, Eds., Springer, Berlin, (1996), pp. 327–334, Lecture Notes in Computer Science 1196. G. Goos, J. Hartmanis and J. van Leeuwen Eds.

[34] Lebedev, V.I., *Russ. J. Numer. Ansl. Math. Modelling*, 13(2):107–116 (1998).

[35] Medovikov, A.A., *BIT*, 38(2):372–390 (1998).

[36] Golushko, M.I., and Novikov, E.A., *Russ. J. Numer. Anal. Math. Modelling*, 14(1):71–85 (1999).

[37] Abdulle, A., *BIT*, 40(1):177–182 (2000).

[38] Sommeijer, B.P., and der Houwen, P.J. Van, *ZAMM*, 61:105–114 (1981).

[39] Bakker, M., Technical Note TN 62, Mathematical Center, Amsterdam, (1971) (in Dutch).

[40] van der Houwen, P.J., CWI Report NM-R9420, CWI, Amsterdam, (1994).

[41] Guillou, A., and Lago, B., *Recherche de formules a grand rayon de stabilité*, Ier Congr. Assoc. Fran. Calcul, AFCAL, Grenoble, Sept. 1960, pp. 43–56, (1961).

[42] Majda, A., and Sethian, J., *Comb. Sci. and Technology*, 42:185–205 (1985).

[43] Schlichting, H., *Boundary-Layer Theory*, McGraw-Hill, New York, 7^{th} edition, (1979).

[44] Williams, F.A., *Combustion Theory*, Addison-Wesley, New York, 2nd edition, (1985).

[45] Mason, E.A., and Saxena, S.C., *Phys. Fluids*, 5:361–369 (1958).

[46] Warnatz, J., Maas, U., and Dibble, R.W., *Combustion: Physical and Chemical Fundamentals, Modeling and Simulation, Experiments, Pollutant Formation*, Springer-Verlag, Berlin, (1996).

[47] Kee, R.J., Dixon-Lewis, G., Warnatz, J., Coltrin, M., and Miller, J., Sandia Report SAND86-8246, Sandia National Labs., Livermore, CA, (1986).

[48] Chorin, A.J., *J. Comput. Phys.*, 2:12–26 (1967).

[49] Bell, J.B., and Marcus, D.L., *J. Comput. Phys.*, 101:334–348 (1992).

[50] Almgren, A.S., Bell, J.B., Colella, P., Howell, L.H., and Welcome, M., *J. Comput. Phys.*, 142:1–46 (1998).

[51] Schneider, T., Botta, N., Geratz, K. J., and Klein, R., *J. Comput. Phys.*, 155:248–286 (1999).

[52] McMurtry, P.A., Jou, W.-H., Riley, J.J., and Metcalfe, R.W., *AIAA J.*, 24(6):962–970 (1986).

[53] Rutland, C., Ferziger, J.H., and Cantwell, B.J., Report TF-44, Thermosciences Div., Mech. Eng., Stanford Univ., Stanford, CA, (1989).

[54] Rutland, C.J., and Ferziger, J.H., *Combustion and Flame*, 84:343–360 (1991).

[55] Mahalingam, S., Cantwell, B.J., and Ferziger, J.H., *Physics of Fluids A*, 2:720–728 (1990).

[56] Brown, P.N., Byrne, G.D., and Hindmarsh, A.C., *SIAM J. Sci. Stat. Comput.*, 10:1038–1051 (1989).

[57] Najm, H.N., in *Transport Phenomena in Combustion* (S. Chan, Ed., volume 2, Taylor and Francis, Wash. DC, pp. 921–932, (1996).

[58] Najm, H.N., and Wyckoff, P.S., *Combustion and Flame*, 110(1-2):92–112 (1997).

[59] Vesovic, V., and Wakeham, W.A., *Physica*, 201A:501–514 (1993).

[60] Thijsse, B.J., ‘t Hooft, G.W., Coombe, D.A., Knaap, H.F.P., and Beenakker, J.J.M., *Physica*, 98A:307–312 (1979).

[61] Ern, A., and Giovangigli, V., *Multicomponent Transport Algorithms*, Springer-Verlag, Berlin, (1994).

[62] Mason, E.A., and Monchick, L., *J. Chem. Phys.*, 36:1622–1639 (1962).

[63] Brout, R., *J. Chem. Phys.*, 22:1189–1196 (1954).

Distribution

Printed copies sent through the mail

1 Prof. Omar M Knio
Dept. of Mechanical Engineering
103 Latrobe Hall
The Johns Hopkins University
Baltimore, MD 21218-2686

1 Dr. Philip Paul
Eksigent Technologies, LLC
2021 Las Positas Cr., Ste 161
Livermore, CA 94551

1 Prof. Uwe Riedel
IWR - Ruprecht-Karls-University Heidelberg
Im Neuenheimer Feld 368
D-69120 Heidelberg, Germany

1 Dr. Leland M Jameson
Lawrence Livermore National Laboratory
PO Box 808, MSL-22
Livermore, CA 94551

1 Dr. Gopal Patnaik
Code 6410
Naval Research Laboratory
4555 Overlook Ave.
Washington, DC 20375

1 Prof. Grégoire S Winckelmans
Universite Catholique de Louvain
Batiment Stevin,
Place du Levant 2
B-1348 Louvain-la-Neuve
Belgium

1 Prof. Eric Darve
Stanford University
Durand Building
Room 265
Stanford, CA 94305-4040

1 Dr. Terese Løvås
University of Cambridge
Department of Engineering
Trumpington Street
Cambridge CB2 1PZ, UK

1 Prof. Markus Kraft
University of Cambridge
Department of Chemical Engineering
New Museums Site
Pembroke Street
Cambridge CB2 3RA UK

1 Dr. Jean-Pierre Hathout
Robert Bosch Corporation
RTC
4009 Miranda Ave
Palo Alto, CA 94304

1 Prof. Ahmed Ghoniem
MIT, Rm 3-342
77 Mass Ave.
Cambridge, MA 02139

1 Prof. Alexandre Chorin
Mathematics Dept.
UC Berkeley
Berkeley, CA 94720

1 Prof. Ishwar K. Puri
University of Illinois at Chicago
Department of Mechanical Engineering (M/C 251)
842 W. Taylor St., 2039 ERF
Chicago, IL 60607-7022

1 Prof. Dimitris Goussis
ICEHT, PO Box 1414
26500 Patras, Greece

1 Prof. Mauro Valorani
Departimento di Meccanica e Aeronautica
Via Eudossiana, 18 - 00184 Roma
Italy

1 Prof. Tarek Ecekki
Mechanical and Aerospace Engineering
4152 Broughton Hall
2601 Stinson Drive
North Carolina State University
Raleigh, NC 27695-7910

1 Prof. Roger Ghanem
Dept. of Civil Engineering
The Johns Hopkins University
Baltimore, MD 21218-2686

1 Prof. Olivier Le Maitre
Universite d'Evry Val d'Essonne
Centre d'Etudes de m'ecanique d'Ile de France
40 rue du Pelvoux CA 1455
91020 Evry cedex
France

1 Dr. Mark Carpenter
NASA Langley Research Center
MS 254
Hampton, VA 23681-2199

1 Prof. Ernst Hairer
Section de Mathematiques
2-4 Rue du Lievre
CH-1211 Geneve 24
Switzerland

1 Dr. Stephen Thomas
Scientific Computing Division
National Center for Atmospheric Research
1850 Table Mesa Drive
Boulder, CO 80305

1 Prof. Jan Verwer
University of Amsterdam, Faculty of Science
Korteweg-de Vries Institute KDV
Plantage Muidergracht 24
1018 TV Amsterdam, The Netherlands

1 Prof. Stephen B. Pope
Sibley School of Mechanical and Aerospace Engineering
240 Upson Hall
Cornell University
Ithaca, NY 14853-7501

1 Prof. Michael Frenklach
Mechanical Engineering
6161 Etcheverry Hall
University of California
Berkeley, CA 94720-1740

1 Prof. Alexandre Ern
Centre D'Enseignement et de Recherche en Mathematique
Informatique et Calcul Scientifique Cermics - ENPC
6et 8, avenue Blaise Pascal
Cite Descartes - Champs-sur-Marne
77455 Marne-La-Vallee Cedex 2, France

20	MS9051	Habib N. Najm
1	MS1111	John Shadid
1	MS0826	Steve Kempka
1	MS1111	Karen Devine
1	MS9042	Christopher Moen
1	MS9051	Andrew McIlroy
3	MS9018	Central Technical Files, 8945-1
1	MS0899	Technical Library, 9616
1	MS9021	Classification Office, 8511/Technical Library, MS 0899,9616 DOE/OSTI via URL